J. Fluid Mech. (1988), *vol.* 194, *pp.* 333–349
Printed in Great Britain

The dynamics of freely decaying two-dimensional turbulence

By M. E. BRACHET†‖, M. MENEGUZZI‡, H. POLITANO‖, AND P. L. SULEM‖¶

†CNRS, G.P.S., Ecole Normale Supérieure 24 rue Lhomond, 75231 Paris Cedex 05, France
‡CNRS, Service d'Astrophysique, C.E.N.-Saclay, 91191 Saclay, France
‖CNRS, Observatoire de Nice, B.P. 239, 06007 Nice Cedex, France
¶School of Mathematical Sciences, Tel-Aviv University, 69978 Tel Aviv, Israel

(Received 25 August 1987 and in revised form 4 January 1988)

Direct numerical simulations of decaying high-Reynolds-number turbulence are presented at resolutions up to 800^2 for general periodic flows and 2048^2 for periodic flows with large-scale symmetries. For turbulence initially excited at large scales, we characterize a transition of the inertial energy-spectrum exponent from $n \approx -4$ at early times to $n \approx -3$ when the turbulence becomes more mature. In physical space, the first regime is associated with isolated vorticity-gradient sheets, as predicted by Saffman (1971). The second regime, which is essentially statistical, corresponds to an enstrophy cascade (Kraichnan 1967; Batchelor 1969) and reflects the formation of layers resulting from the packing of vorticity-gradient sheets. In addition to these small-scale structures, the simulation displays vorticity macro-eddies which will survive long after the vorticity-gradient layers have been dissipated (McWilliams 1984). We validate the linear description of two-dimensional turbulence suggested by Weiss (1981), which predicts that coherent vortices will survive in regions where vorticity dominates strain, while vorticity-gradient sheets will be formed in regions where strain dominates. We show that this analysis remains valid even after vorticity-gradient sheets have been formed.

1. Introduction

Much effort has been devoted during the last decade to two-dimensional incompressible turbulence governed by the Navier–Stokes equation

$$\left.\begin{aligned} &\partial_t \boldsymbol{v} + (\boldsymbol{v}\cdot\boldsymbol{\nabla})\,\boldsymbol{v} = -\boldsymbol{\nabla} p + \nu\boldsymbol{\nabla}^2\boldsymbol{v}, \\ &\boldsymbol{\nabla}\cdot\boldsymbol{v} = 0, \\ &\text{initial and boundary value.} \end{aligned}\right\} \tag{1.1}$$

Although physical flows are usually three-dimensional, two-dimensional turbulence is often considered as a first approximation when modelling global circulation in the atmosphere or ocean where motions evolve with horizontal scales much larger than the thickness of the fluid. Furthermore, at large Reynolds numbers, two-dimensional turbulence displays interesting specific properties. Indeed, the vorticity $\boldsymbol{\omega} = \boldsymbol{\nabla} \times \boldsymbol{v}$ is perpendicular to the plane of the flow and satisfies

$$\partial_t \boldsymbol{\omega} + (\boldsymbol{v}\cdot\boldsymbol{\nabla})\,\boldsymbol{\omega} = \nu\boldsymbol{\nabla}^2\boldsymbol{\omega}. \tag{1.2}$$

It is thus a (pseudo) scalar $\omega = \partial_x v - \partial_y u$, conserved along the fluid trajectories in the inviscid limit. This prevents vorticity stretching and thus the development of an

energy cascade to the small scales, a central feature of three-dimensional turbulence. In two-dimensions, the mechanism for small-scale generation is the stretching of vorticity gradients. In the inviscid limit, the latter satisfies

$$\partial_t \nabla\omega + (\boldsymbol{v}\cdot\nabla)\nabla\omega = -(\nabla\boldsymbol{v})\cdot\nabla\omega. \tag{1.3}$$

It is also convenient to consider

$$\boldsymbol{\eta} = \nabla\times\boldsymbol{\omega} = \begin{bmatrix} \partial_y \omega \\ -\partial_x \omega \end{bmatrix}, \tag{1.4}$$

which is deduced from $\nabla\omega$ by a rotation of $\frac{1}{2}\pi$ and satisfies

$$\partial_t \boldsymbol{\eta} + (\boldsymbol{v}\cdot\nabla)\boldsymbol{\eta} = \boldsymbol{\eta}\cdot(\nabla\boldsymbol{v}), \tag{1.5}$$

an equation analogous to the one governing vorticity in three dimensions†.

Vorticity conservation and vorticity-gradient production are the basic elements of small-scale dynamics in two-dimensional turbulence. As noticed by Saffman (1971), the advection of vorticity along the fluid trajectories may bring close together different values of ω, producing thin layers between macro-eddies across which vorticity jumps. Such quasi-discontinuities of vorticity along rectilinear structures would lead to an inertial range with a k^{-4} energy spectrum. A different point of view was presented by Kraichnan (1967) and Batchelor (1969) who used a statistical approach. By analogy with the direct energy cascade in three dimensions, they conjectured the existence in two-dimensions of an enstrophy (mean-square vorticity) cascade to the small scales. Phenomenology and dimensional considerations then lead to a k^{-3} inertial energy spectrum (with a possible logarithmic correction suggested by Kraichnan (1971) to take into account the effect of non-local interactions).

The first numerical simulations of two-dimensional turbulence by direct integration of Navier–Stokes equations were made at the end of the sixties and at the beginning of the seventies with a resolution of 32^2 (Lilly 1969, 1971, 1972; Deem & Zabusky 1971). But these resolutions were much too low to enable the authors to isolate an inertial range and definitely discriminate between the two predicted spectral exponents. Later Herring *et al.* (1974), using resolutions up to 128^2, concluded that at least 512^2 modes were required to properly simulate an inertial range. Preliminary calculations at this resolution were presented by Orszag (1977) and the computation showed, when the large-scale Reynolds number was increased from 1100 to 25000, a distinct change from a k^{-4} energy spectrum to a spectrum roughly proportional to k^{-3}.

More recent computations (Fornberg 1977; Basdevant *et al* 1981; McWilliams 1984) suggest that in addition to small scales generated by vorticity-gradient stretching, two-dimensional turbulent flows also display dynamically stable coherent structures corresponding to isolated vorticity concentrations.

In this paper, we present direct numerical simulations of two-dimensional turbulent flows at the highest resolutions which can reasonably be achieved on a Cray-1s computer with one million words in central memory: 800^2 collocation points for general periodic flows and 2048^2 for periodic flows with large-scale symmetries. We concentrate here on the generation of small scales in freely decaying turbulence, excluding the development of the inverse energy cascade predicted by Kraichnan

† Note that in the three-dimensional case only the symmetric part of the matrix of velocity derivatives plays a role, whereas in (1.5) both the symmetric and the antisymmetric parts are present.

(1967) and observed in numerical simulations (Fyfe, Montgomery & Joyce 1977; Frisch & Sulem 1984; Herring & McWilliams 1985). Our main interest is to characterize small-scale generation in two-dimensional turbulence. The paper is organized as follows. In §2, we discuss the numerical algorithms and describe the characteristics and the parameters of the runs. In §3, we concentrate on spectral properties of the solution such as the energy and dissipation spectra, and briefly consider the geometry of the small-scale structures. The dynamics in physical space is presented and interpreted in §4. It concerns both the formation of vorticity-gradient layers and the evolution of vorticity macro-eddies. Section 5 is the conclusion.

2. Numerical algorithm and description of the runs

The flow being assumed 2π-periodic, we have used Fourier spectral methods for the space variables because they are both precise and easy to implement (Gottlieb & Orszag 1977). In the case of general periodic flow the stream function can be written

$$\psi(x,y,t) = \sum_{k_x=0}^{N/2} \sum_{k_y=-N/2}^{N/2} a(\boldsymbol{k},t)\, \mathrm{e}^{\mathrm{i}\boldsymbol{k}\cdot\boldsymbol{x}} + \mathrm{cc}. \tag{2.1}$$

In the case of periodic flows with large-scale symmetries, the stream function has a Fourier representation

$$\psi(x,y,t) = \sum_{k_x=1}^{N/2} \sum_{k_y=1}^{N/2} a(\boldsymbol{k},t) \sin(k_x x) \sin(k_y y), \tag{2.2}$$

where the $a(\boldsymbol{k},t)$ coefficients are non-zero only when k_x and k_y are both even or both odd. This representation, which is compatible with the Navier–Stokes equations, corresponds in physical space to the following symmetries: (i) invariance by rotation of π around the point $x = \frac{1}{2}\pi$, $y = \frac{1}{2}\pi$, (ii) reflectional symmetry on the sides of an impermeable box $x = 0$ and π, $y = 0$ and π. This so-called 'sparse mode technique' was first implemented in Brachet *et al* 1983 for the three-dimensional Taylor–Green vortex. For a given ratio between the larger and the smaller scales retained in the system, this method leads to a significant reduction of both storage and operation number.

The equation for the vorticity is integrated in the form

$$\partial_t \omega + \partial_x(u\omega) + \partial_y(u\omega) = \nu\nabla^2\omega, \tag{2.3}$$

where u and v are the two velocity components.

The time marching is done in Fourier space with a second-order (stabilized) leap-frog Crank–Nicolson scheme of the form:

$$\frac{\omega_{n+1}(\boldsymbol{k}) - \omega_{n-1}(\boldsymbol{k})}{2\delta t} = -\nu\boldsymbol{k}^2 \tfrac{1}{2}[\omega_{n+1}(\boldsymbol{k}) + \omega_{n-1}(\boldsymbol{k})] + F_n(\boldsymbol{k}), \tag{2.4}$$

where $\omega_n(\boldsymbol{k})$ denotes the $\boldsymbol{k}$-vorticity mode at time $n\delta t$ and $F_n(\boldsymbol{k})$ is the Fourier transform of the nonlinear term at time $n\delta t$. $F_n(\boldsymbol{k})$ is computed from $\omega_n(\boldsymbol{k})$ by the following procedure. In Fourier space, the stream function is related to the vorticity by

$$\psi_n(\boldsymbol{k}) = \frac{\omega_n(\boldsymbol{k})}{k^2}, \tag{2.5}$$

Run	S5	P2-800	P8-800	P2-512
Symmetry	Symmetric	General periodic	General periodic	General periodic
Resolution	2048^2	800^2	800^2	512^2
k_0	5	2	8	2
Energy	6×10^{-2}	4×10^{-2}	3×10^{-2}	0.1
Enstrophy	3.6	0.23	1.9	0.5
Viscosity	2.33×10^{-5}	7.5×10^{-5}	10^{-4}	1.5×10^{-4}
CPU/timestep (s)	5.5	2	2	0.6
10/timestep (s)	2.5	5	5	Incore
Timestep	6.25×10^{-4}	2×10^{-3}	10^{-3}	2×10^{-3}
Number of timesteps	20800	30000	44000	15000

TABLE 1. Parameters for the flow simulations

and the Fourier transform of the velocity

$$u = \partial_y \psi, \quad v = -\partial_x \psi$$

reads

$$u_n(\boldsymbol{k}) = \mathrm{i}k_y \psi_n(\boldsymbol{k}), \quad v_n(\boldsymbol{k}) = -\mathrm{i}k_x \psi_n(\boldsymbol{k}). \tag{2.6}$$

After transforming the velocity and the vorticity to physical space, one computes $\alpha_n(\boldsymbol{x}) = u_n(\boldsymbol{x})\omega_n(\boldsymbol{x})$ and $\beta_n(\boldsymbol{x}) = v_n(\boldsymbol{x})\omega_n(\boldsymbol{x})$ at the collocation points. One finally transforms back to Fourier space to calculate $\mathrm{i}k_x\alpha_n(\boldsymbol{k})$, $\mathrm{i}k_y\beta_n(\boldsymbol{k})$ and finally $\omega_{n+1}(\boldsymbol{k})$.

Note that (2.3), which is the two-dimensional version of the classical three-dimensional representation

$$\partial_t \boldsymbol{\omega} = \boldsymbol{\nabla} \times (\boldsymbol{v} \times \boldsymbol{\omega}) + \nu \nabla^2 \boldsymbol{\omega}, \tag{2.7}$$

has the advantage of enforcing energy conservation by the nonlinear terms for truncated Fourier series. Enstrophy may also be exactly preserved by suppressing aliasing errors, using a spectral truncation for wavenumbers $k_{\mathrm{M}} \geqslant \frac{1}{3}N$, where N is the total number of modes in each direction.

In all the simulations reported here, we used Gaussian (pseudo)-random initial data, such that the energy spectrum

$$E(k) = \frac{1}{2} \sum_{k-\frac{1}{2} < |\boldsymbol{k}'| < k+\frac{1}{2}} |\boldsymbol{v}(\boldsymbol{k}')|^2, \tag{2.8}$$

is initially given by

$$E_0(k, t=0) = Ck \exp\left(-(k/k_0)^2\right). \tag{2.9}$$

The simulations presented in this paper are listed in table 1. Each of these runs requires tens of hours of supercomputer time. They thus have been preceded by simulations at lower resolutions to adjust the parameters and get a quick look at the phenomena. The results obtained on general periodic flows at resolutions up to 512^2 and on an S-5-like symmetric flows at 1024^2-resolution were published in Brachet & Sulem (1984, 1985), Brachet, Meneguzzi & Sulem (1985, 1986). A two-dimensional flow with even more symmetries than S-5 was considered by Kida (1985) who simulated it using our in-core-1024^2-code.

3. Evolution of spectral and integral quantities

Among the significant integral quantities that describe the development of a two-dimensional turbulence initially concentrated in the large scales, one can consider the (two-dimensional) skewness and the enstrophy dissipation. The two-dimensional skewness $\mathscr{S}$, which is a non-dimensional measure of the rate of production of mean-square vorticity gradients by nonlinear effects, is defined as follows (Herring *et al.* 1974). Let

$$T_\omega(k) = \sum_{k-\frac{1}{2}<|k'|<k+\frac{1}{2}} \sum_{k''} |\omega(-\boldsymbol{k}')\, \boldsymbol{v}(\boldsymbol{k}'-\boldsymbol{k}'')\cdot \mathrm{i}\boldsymbol{k}''\omega(\boldsymbol{k}'')|, \tag{3.1}$$

denote the enstrophy transfer through the k-shell at time t. Then

$$\mathscr{S} = \frac{\Sigma_k k^2 T_\omega(k)}{\Sigma_k k^4 E(k)\,[\Sigma_k k^2 E(k)]^{\frac{1}{2}}}. \tag{3.2}$$

In terms of physical quantities, $\mathscr{S}$ also reads

$$\mathscr{S} = -2\frac{\langle \partial_x u(\partial_x \omega)^2 \rangle}{\langle (\partial_x u)^2 \rangle^{\frac{1}{2}} \langle (\partial_x \omega)^2 \rangle}. \tag{3.3}$$

Figure 1 (*a*) shows the evolution of the skewness for the run S5. We see that after an early rapid growth corresponding to the period of small-scale generation, $\mathscr{S}$ reaches a maximum around $t = 1$ and then decays slowly. Figure 1 (*b*) shows the evolution of the enstrophy dissipation

$$\Sigma = \nu \int (\boldsymbol{\nabla} \times \boldsymbol{\omega})^2 \,\mathrm{d}\boldsymbol{x}. \tag{3.4}$$

It reaches a maximum at a time $t \approx 6$ (significantly later than the skewnes maximum), and then decays. These two maxima define two characteristic times for the development of two-dimensional turbulence, as we shall now see by considering the energy spectrum (2.7) whose evolution is generally used as a diagnostic of small-scale generation.

The energy spectrum of developed turbulence is expected to display a power-law inertial range and an exponential tail which reflects the spatial analyticity of the solutions of Navier–Stokes equations. After the early inviscid period, this exponential range is generally referred to as the dissipation range. In order to extract quantitative information about the power-law exponent and the high-wavenumber exponential decay, we have resorted to analysing the energy spectrum in terms of an assumed functional form. We fit the energy spectrum with a function $A(t)\, k^{-n(t)} \exp(-\beta(t)\, k)$. In this way, we estimate both the smallest significantly excited scale by the logarithmic decrement β (Sulem, Sulem & Frisch 1983; Frisch *et al* 1983; Brachet *et al.* 1983), and the spectral exponent n.

Figure 1 (*c*) shows that the early time dynamics is characterized by an exponential decay of the logarithmic decrement. This process stops when skewness reaches its maximum. At this time, scales small enough to make viscosity efficient have been excited. Vorticity-gradient production is then inhibited and the width of the analyticity strip $\delta(t) \approx \frac{1}{2}\beta(t)$ of the Navier–Stokes solution stabilizes. Just after the logarithmic-decrement stabilization, the spectral exponent is close to the value $n = -4$ (figure 1*d*), predicted by the Saffman (1971) theory. Later, around the time of maximum enstrophy dissipation ($t \approx 6$), the spectral exponent displays a sharp transition to a value close to $n = -3$, a value consistent with the enstrophy cascade (Kraichnan 1967); Leith 1968; Batchelor 1969; Pouquet *et al.* 1975). We note on

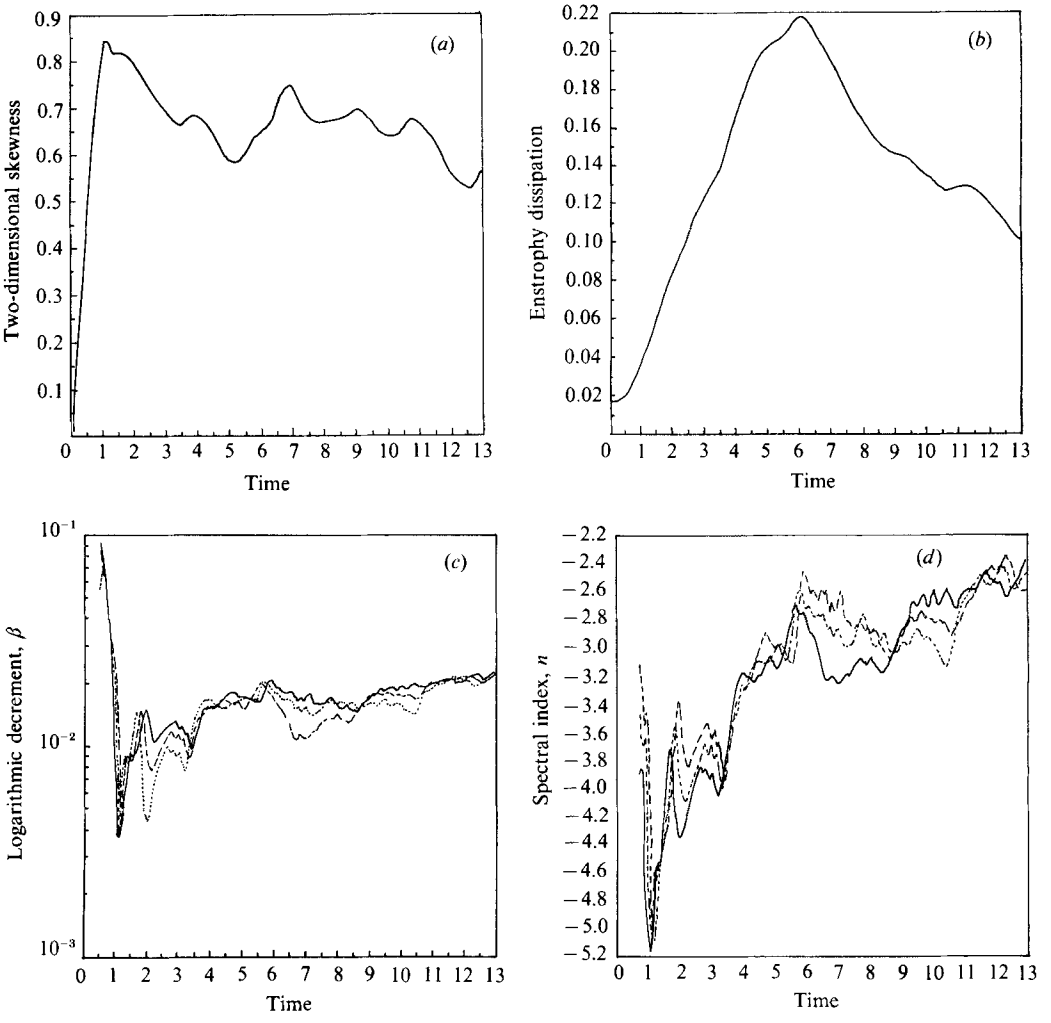

FIGURE 1. Spectral evolution of run S5 (see table 1): (*a*) skewness, (*b*) total enstrophy dissipation, (*c*) logarithmic decrement β and (*d*) spectral exponent n of the energy spectrum versus time. For (*c*, *d*) each curve corresponds to a different fit wavenumber range covering the inertial and part of the dissipative range; the dispertion gives an idea of the precision of the n and β determination.

figure 1 (*d*), that by the end of the run ($9 < t < 13$), the prefactor tends to increase slowly in absolute value. This effect is probably related to the significant dissipation which has then occurred. This is visible on figure 1 (*b*) and also on figure 1 (*c*), where the dissipation scale and thus the extension of the inertial range have been reduced significantly. Similar observations can be made for the non-symmetric runs. Figure 2 (*a*) for example shows the spectral index versus item for the run P2-800. The best fit, represented by the solid line, corresponds to the range $5 < k < 40$. The other fits are obtained on ranges that are significantly larger than the inertial range and thus more affected by the algebraic prefactor of the dissipation range. The extension of the inertial range is visible on figues 2 (*b*) and 2 (*c*) which display the compensated energy spectra $k^4E(k)$ and $k^3E(k)$ at times before and after the transition, respectively. Note the large extent of the dissipation range, necessary in order to accurately represent all the scales of motion that contribute appreciably to the enstrophy

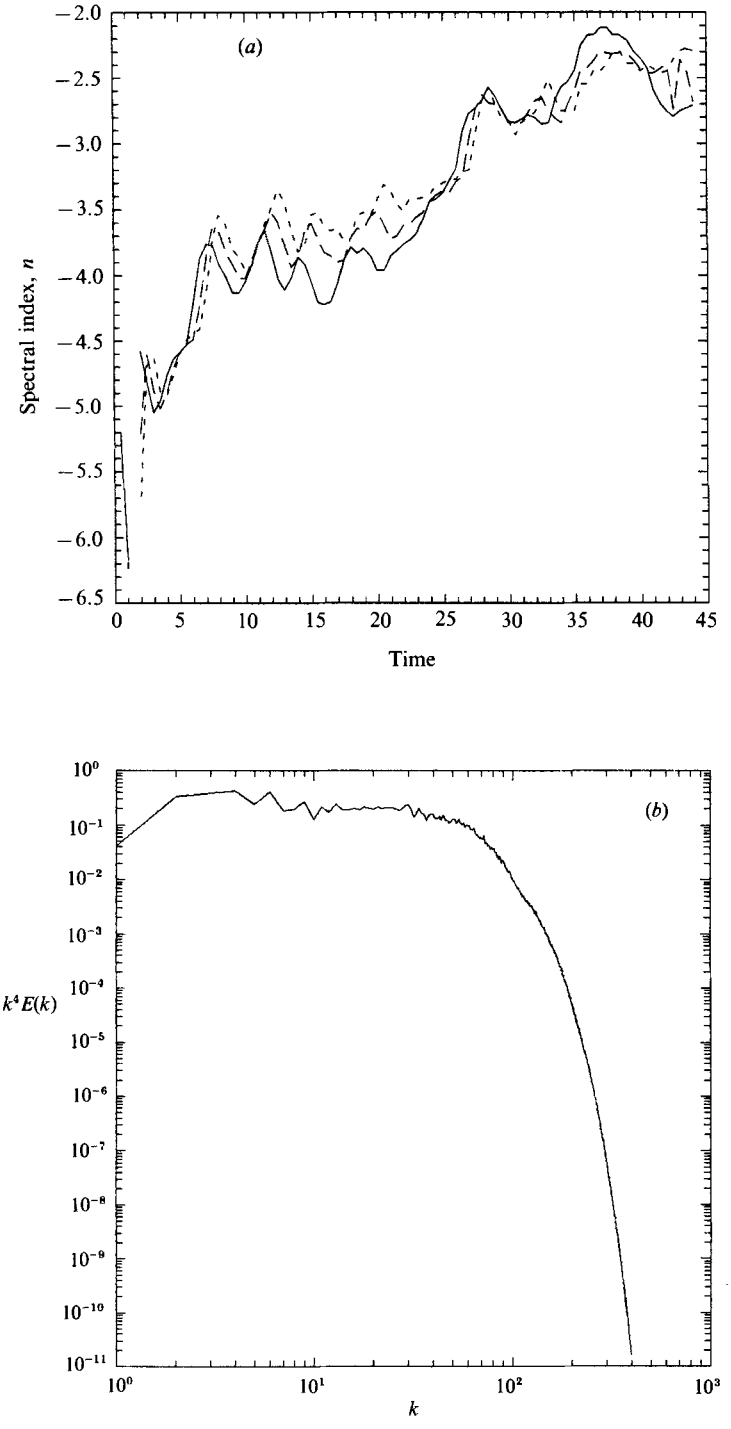

FIGURE 2(*a*, *b*). For caption see next page.

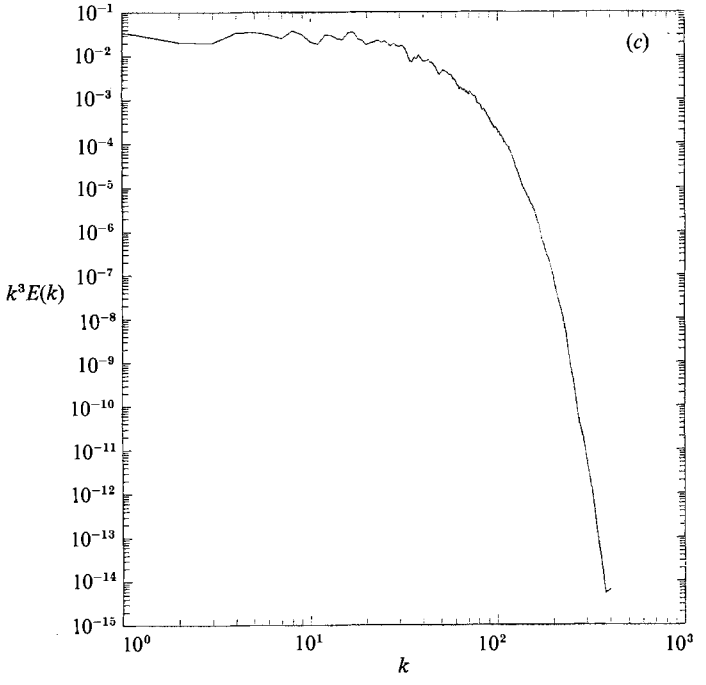

FIGURE 2. Spectral evolution of run P2-800 (see table 1). (*a*) Spectral index n versus time obtained by fitting the energy spectrum with a function $E(k) = Ck^n \exp(-\beta k)$ in three different wavenumber ranges: ———, $3 < k < 40$; – – –, $3 < k < 60$; · · · ·, $3 < k < 80$. (*b*) $k^4E(k)$ versus k at $t = 13$. (*c*) $k^3E(k)$ versus k at $t = 40$.

dissipation. In practice, in all the computations presented here, we adjusted the viscosity in such a way as to make the energy-spectrum logarithmic decrement (or the dissipation scale) be at least eight times larger than the mesh size.

In a two-dimensional flow, the times of maximum skewness and maximum dissipation go to infinity as the Reynolds number R increases to infinity. Several predictions have been made concerning the asymptotic scaling of the time of maximum dissipation with the Reynolds number. They suggest that the scaling is like $\log R$ or some fractional power of this quantity (Kida 1981, 1985; Tatsumi & Yanase 1981; Lesieur 1987). Such a slow variation seems difficult to investigate by direct numerical simulations where the accessible range of Reynolds numbers producing developed turbulence is very limited. Similarly, it is difficult to test the t^{-2} enstrophy decay law predicted by Batchelor (1969).

As seen on the isovorticity contours displayed in figure 3, the k^{-4} and k^{-3} regimes correspond to quite different configurations of the small-scale structures in physical space. During the k^{-4} phase, the small-scale structures consist of isolated quasi-rectilinear vorticity-gradient sheets resulting from differential advecttion of initial vortices and stretching of vorticity gradients by velocity gradients. In the k^{-3} regime, the early time sheets have been packed together and display a complex structure (figure 3*b*). We also notice that in addition to the vorticity-gradient sheets, figure 3 displays survival vortices which can be traced back to the initial conditions.

The dynamics in physical space will be described and interpreted in detail in §4, where more elaborate visualizations will be presented. Here we only point out that the mechanisms of vorticity-gradient formation and of their piling up when the

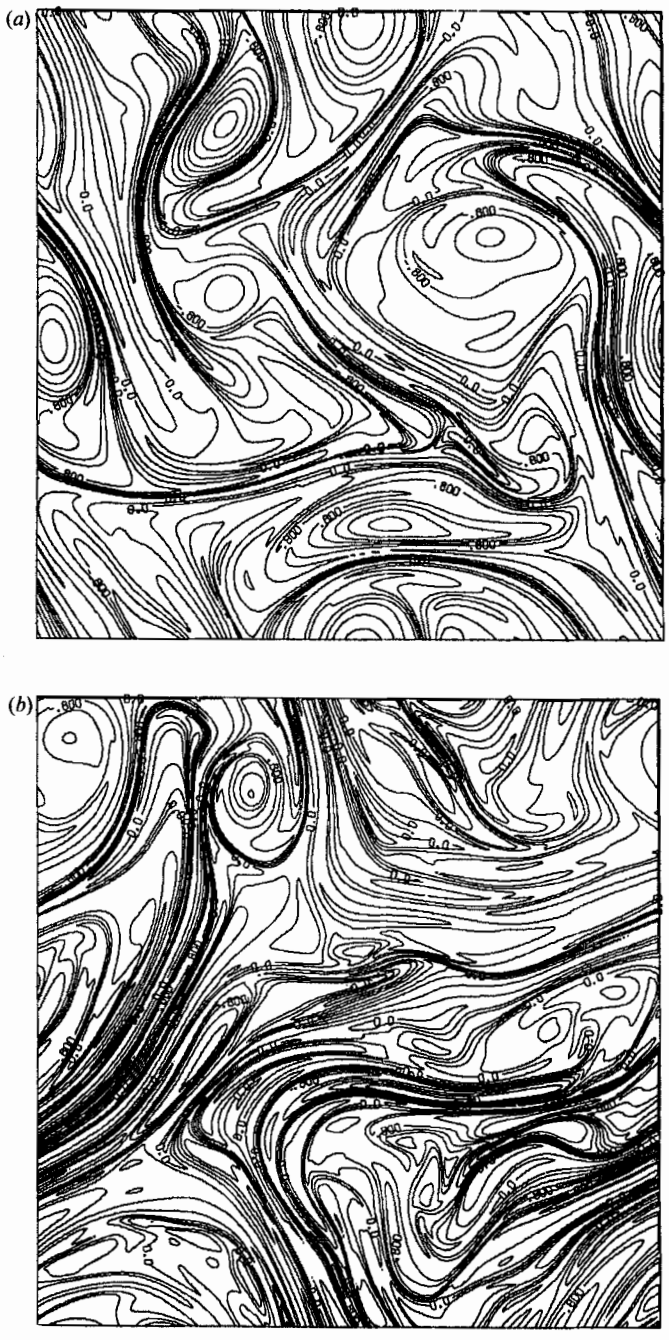

FIGURE 3. Isovorticity lines for run P2-800: (*a*) $t = 13$, (*b*) $t = 40$.

turbulence becomes more mature are not significantly affected by the periodicity constraint. This is demonstrated on figure 4 which displays the regimes of isolated and packed sheets for the P8-800 run, whose integral scale is much smaller than the box periodicity. We see that the structures are essentially the same as in the run P2-800, and that, in particular, the sheets do not tend to stretch out indefinitely.

We conclude this section by a few remarks on intermittency. Because of the linear

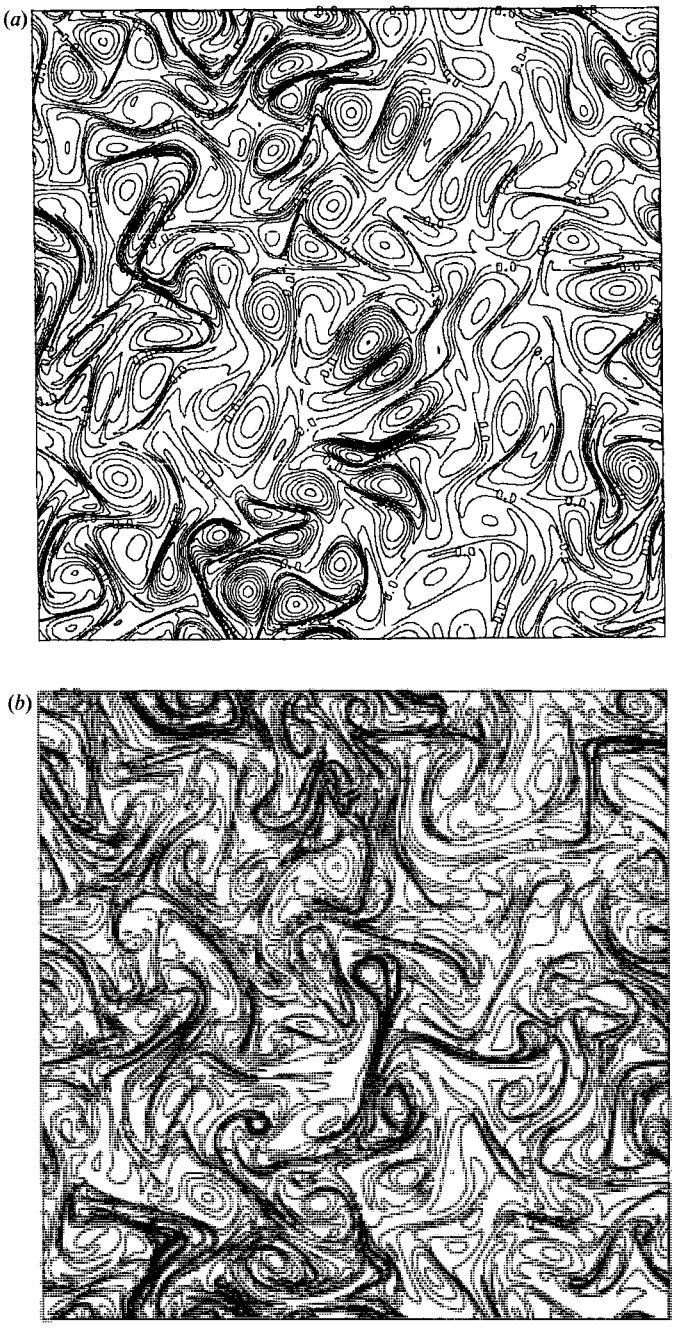

FIGURE 4. Isovorticity lines for run P8-800 (see table 1): (*a*) $t = 4$, (*b*) $t = 10$.

character of the enstrophy cascade which will be discussed in the next section, intermittency in the small scales is not expected to cause deviation from the k^{-3} energy spectrum (Kraichnan 1975). The non-locality of the enstrophy cascade was questioned by Basdevant *et al.* (1981) on the basis of numerical simulations at moderate resolution with hyperviscosity, which display an energy spectrum steeper than k^{-3}. Recent computations by Legras, Santangelo & Benzi (1988) show that the

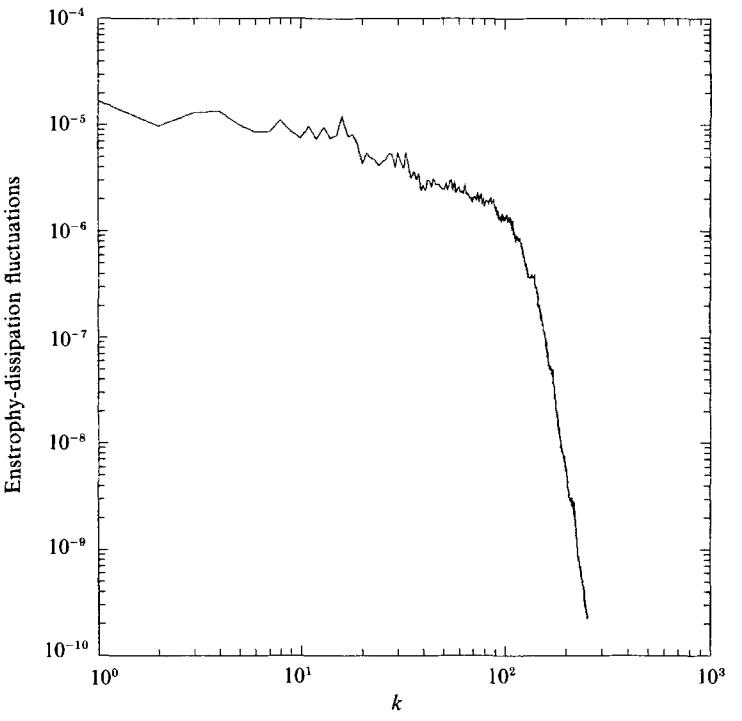

FIGURE 5. Spectrum of the fluctuations of enstrophy dissipation for run P2-512 (see table 1) at time $t = 15.5$.

scale separation of these simulations was insufficient to display an enstrophy cascade and that the observed spectrum was dominated by the coherent vortices (Benzi, Patarnello & Santangelo 1987). Direct access to intermittency is provided by analysing the local enstrophy dissipation

$$\sigma(\boldsymbol{x}) = \nu(\boldsymbol{\nabla} \times \boldsymbol{\omega})^2. \tag{3.5}$$

Figure 5 shows the dissipation spectrum

$$E_\sigma(k) = \frac{1}{2} \sum_{k-\frac{1}{2} < |\boldsymbol{k}'| < k+\frac{1}{2}} |\sigma(\boldsymbol{k})|^2, \tag{3.6}$$

in the case of run P2-512 at a time $t = 15.5$, corresponding to the k^{-3} regime for the energy spectrum. $E_\sigma(k)$ displays a power-law range $k^{-\alpha}$ with an exponent $\alpha \approx 0.5$. This corresponds to a correlation

$$< \sigma(\boldsymbol{x})\, \sigma(\boldsymbol{x}+\boldsymbol{r}) > \sim |\boldsymbol{r}|^{-\mu}, \tag{3.7}$$

with $\mu = 1-\alpha$. In a simple model where turbulence is fractally homogeneous with a fractal dimension D, structures of scale r occupy a fraction of the total volume which scale like r^{D-2}, which leads to $D = 2-\mu$. More complex relations are obtained in more elaborated models where dissipation is not uniformly distributed over structures of comparable size (Mandelbrot 1976).

4. Physical-space dynamics

One of the main interesting features of direct numerical simulations is that, when visualized, they give a complete picture of the turbulent flow. For our two-dimensional flows, we used a VICOM Raster image processor. In Brachet *et al.* (1986), we have presented the detailed evolution of the vorticity field for the S5-symmetric run. Because of lack of space, we cannot reproduce this evolution here and shall only show a few examples at times that display significant features of the dynamics.

The initial conditions correspond to a few isotropic vortices of positive and negative signs. At $t = 3$ (figure 6*a*, plate 1), a time for which the energy spectrum displays a k^{-4} range, we observe thin and isolated layers across which vorticity changes drastically. As suggested by Saffman (1971), these sheets may be viewed as boundary layers between large-scale eddies. We also see that these layers correspond to vortex tails produced by stretching of vorticity gradients.

It is possible to characterize the regions where vorticity-gradient sheets will be formed: following Weiss (1981) we assume a (temporal and spatial) scale separation between velocity and vorticity gradients. In other words, $\boldsymbol{\nabla v}$ is assumed to be frozen as far as the dynamics of $\boldsymbol{\nabla} \times \boldsymbol{\omega}$ is concerned. Equation (1.5) then becomes linear in Lagrangian coordinates and the evolution of $\boldsymbol{\nabla} \times \boldsymbol{\omega}$ is prescribed by the spectral properties of the velocity gradient. It is convenient to rewrite $\boldsymbol{\nabla v}$ in terms of the strain, $\boldsymbol{S} = \boldsymbol{\nabla v} + \boldsymbol{\nabla v}^{\mathrm{tr}}$ and the vorticity:

$$\boldsymbol{\nabla v} = \frac{1}{2}\begin{pmatrix} S_{11} & S_{12}+\omega \\ S_{12}-\omega & -S_{11} \end{pmatrix}, \tag{4.1}$$

where $S_{11} = 2\partial_x u = -2\partial_y v, S_{12} = \partial_x v + \partial_y u$, and $\omega = \partial_x v - \partial_y u$. The eigenvalues of $\boldsymbol{\nabla v}$ then read

$$\lambda_{\pm} = \pm[-\det(\boldsymbol{\nabla v})]^{\frac{1}{2}} = \pm\tfrac{1}{2}[S_{11}^2 + S_{12}^2 - \omega^2]^{\frac{1}{2}}. \tag{4.2}$$

This equation shows that according to the relative importance of strain and vorticity, the eigenvalues of $\boldsymbol{\nabla v}$ will be real or purely imaginary. In the regions where strain dominates, vorticity gradients are stretched, leading to the formation of vorticity-gradient sheets. In these regions, the motion is said to be hyperbolic. In contrast, in the regions where vorticity dominates, vortices will be stable. In these regions the motion is said to be elliptic. Note that the zero-vorticity lines play a special role. In their neighbourhood, the motion is hyperbolic and vorticity-gradient sheets will be formed. It is thus expected that vorticity gradients will be stretched in the region where the $\boldsymbol{\nabla v}$-eigenvalues are real, leading to the formation of vorticity-gradient sheets directed along the left eigenvector of $\boldsymbol{\nabla v}$ associated with the positive eigenvalue. From (1.3) the direction perpendicular to the sheets is given by the right eigenvector of $\boldsymbol{\nabla v}$ associated with the negative eigenvalue. These (unnormalized) left and right eigenvectors are given by (see (4.1))

$$\left.\begin{aligned} \boldsymbol{l}^{(+)} &= [S_{12}-\omega, (S_{11}^2+S_{12}^2-\omega^2)^{\frac{1}{2}} - S_{11}] \\ \boldsymbol{r}^{(-)} &= \begin{bmatrix} -\omega - S_{12} \\ (S_{11}^2+S_{12}^2-\omega^2)^{\frac{1}{2}} + S_{11} \end{bmatrix}. \end{aligned}\right\} \tag{4.3}$$

In order to test this analysis based on the scale-separation hypothesis, figure 6(*b*) (plate 1) shows $-\det(\boldsymbol{\nabla v})$. We see that it is positive in the regions where the sheets are formed and negative in the regions where the centres of the vortices are located. This permits us to define precisely the core and the tail of a vortex: the core is the

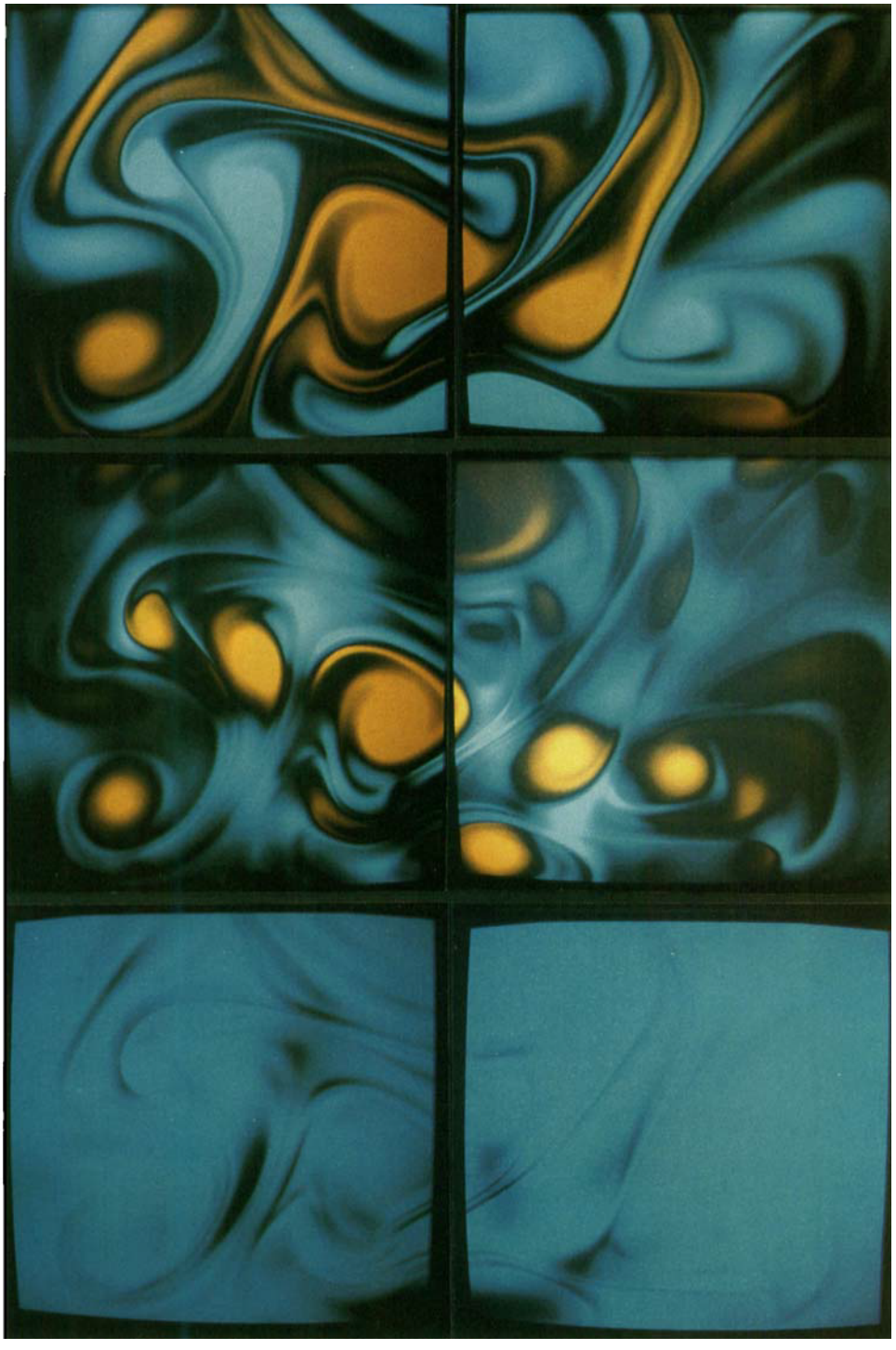

FIGURE 6. Physical-space visualizations for run S5 at $t = 3$ using Raster techniques on a VICOM machine. (*a*) Vorticity ω; (*b*) $-$ det $(\nabla \boldsymbol{v})$; (*c*) strain $-$ det $(\frac{1}{2}(\nabla \boldsymbol{v} + \nabla \boldsymbol{v}^{\mathrm{T}}))$. Negative regions are coloured in orange and positive regions in blue. The intensity is proportional to the absolute magnitude of the field.

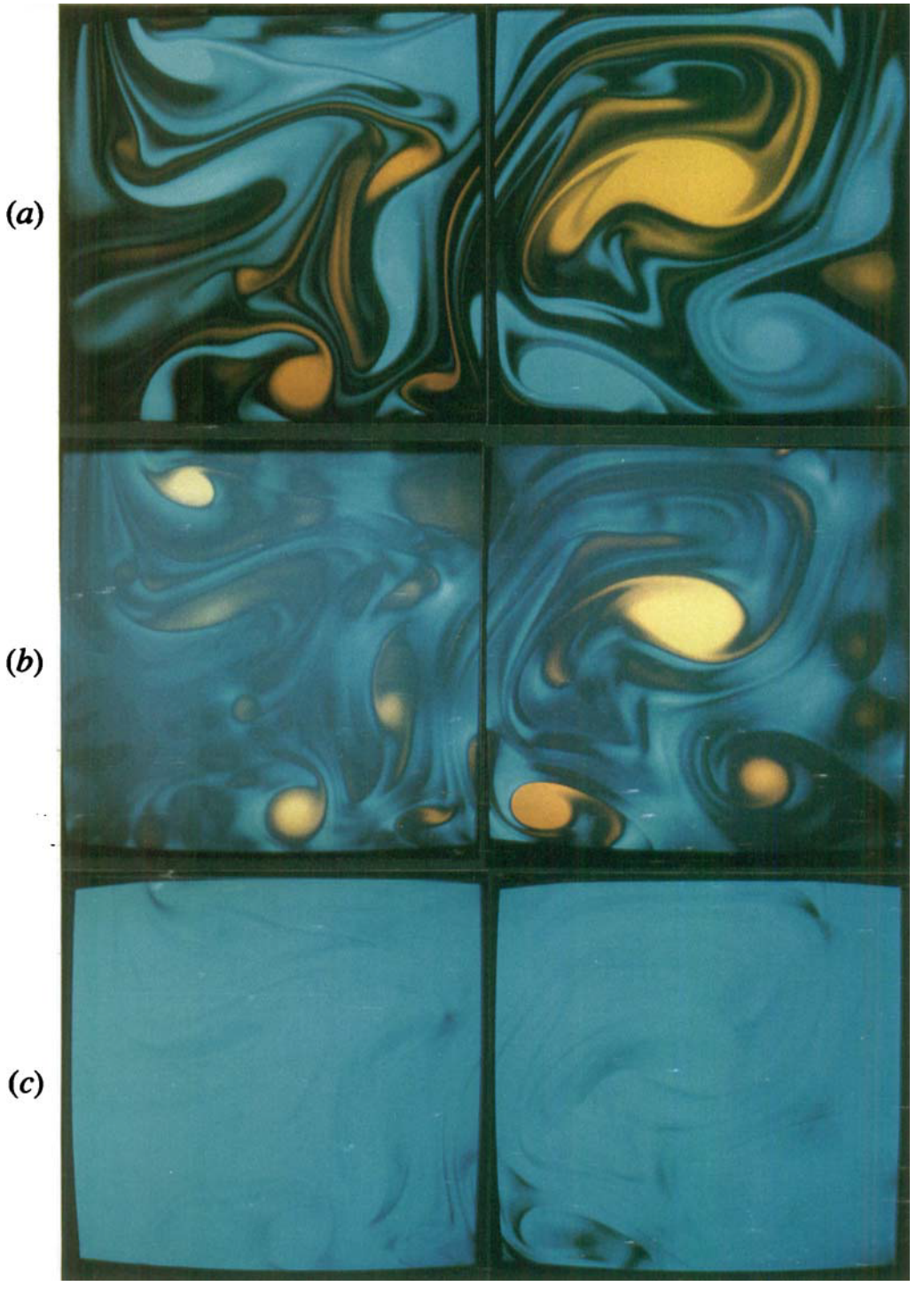

FIGURE 7. Same as figure 6 but at $t = 8$.

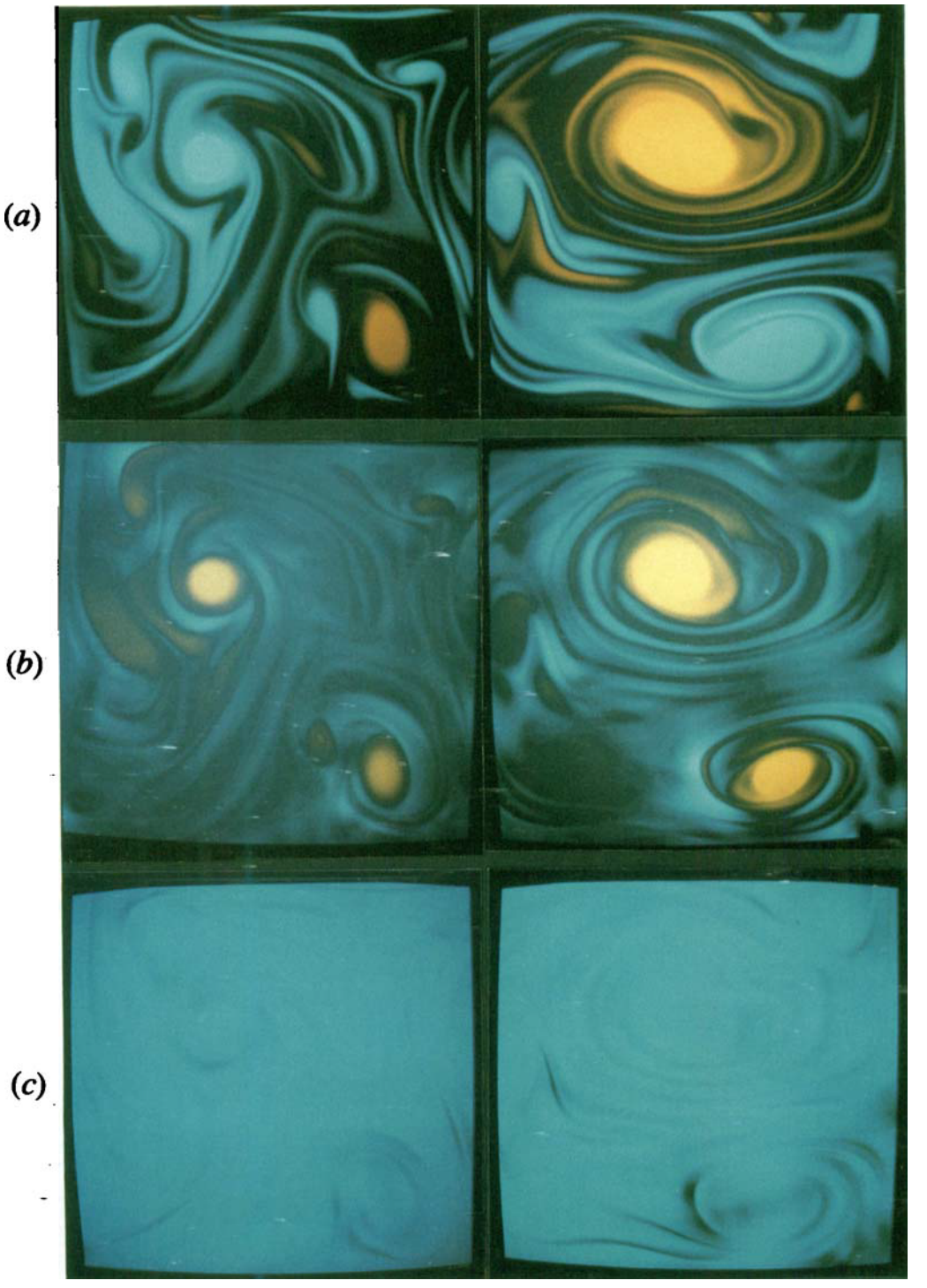

FIGURE 8. Same as figure 6 but at $t = 13$.

region where $-\det(\nabla \boldsymbol{v})$ is negative, the tail is the region where it is positive and thus subject to vortex stretching. Furthermore, we note that $\det(\nabla \boldsymbol{v})$ varies smoothly across the sheets, which is consistent with the assumption of scale separation.

The importance in two-dimensional turbulence of direct straining of small scales by large scales was first pointed out by Kraichnan (1975) and Herring (1975) who argued that *at small scales* the (scalar) vorticity field is passively strained by the large scales.

Figure 6(*c*) (plate 1) shows the distribution of the strain at the same time $t = 3$. We see that the regions of strong strain are those where the sheets develop. However, note that the sheet contributes strongly to the strain distribution.

The usefulness of the Weiss' frozen-velocity-gradient model in explaining sheet formation was noted by McWilliams (1984) and Brachet & Sulem (1984, 1985). However, when the sheets have been formed, they obviously modify the velocity gradients. We shall show that this modification is irrelevant for the sheet dynamics. Indeed, assume that a quasi-one-dimensional layer has been formed in the direction of the left eigenvector associated with the positive eigenvalue of the background velocity gradient (4.1). Denote by ψ_{I} the perturbation of the background stream function induced by these vorticity gradient sheets. As the sheets are quasi-rectilinear, ψ_{I} varies only, at leading order, in the direction perpendicular to the sheets. Thus $\psi_{\mathrm{I}} = \psi_{\mathrm{I}}(s)$, where $s = \boldsymbol{r}(-)\cdot\boldsymbol{x}$. The velocity gradient is changed to

$$\nabla(\boldsymbol{v}+\boldsymbol{v}_{\mathrm{I}}) = \frac{1}{2}\begin{pmatrix} S_{11} & S_{12}+\omega \\ S_{12}-\omega & -S_{11} \end{pmatrix} + \begin{pmatrix} r_x^{(-)} r_y^{(-)} & r_x^{(-)2} \\ r_y^{(-)2} & r_x^{(-)} r_y^{(-)} \end{pmatrix} \frac{\mathrm{d}^3\psi_{\mathrm{I}}}{\mathrm{d}s^2}(s). \tag{4.4}$$

A little algebra then shows that the eigenvalues and eigenvectors of $\nabla(\boldsymbol{v}-\boldsymbol{v}_{\mathrm{I}})$ are identical to those of $\nabla \boldsymbol{v}$. This result is best understood by changing to the orthonormal frame with x-axis along $\boldsymbol{r}^{(-)}$ and y-axis along $\boldsymbol{l}^{(+)}$. In this frame the sheet is directed along the y-axis, and the values of the strain components are such that (see (4.2) and (4.3)) $S_{11} = -(S_{11}^2 + S_{12}^2 - \omega^2)^{\frac{1}{2}}$, $S_{12} - \omega = 0$. At leading order ψ_{I} depends on x only and (4.7) reads

$$\nabla(\boldsymbol{v}+\boldsymbol{v}_{\mathrm{I}}) = \frac{1}{2}\begin{pmatrix} S_{11} & 2\omega - \nabla^2(\psi_{\mathrm{I}}) \\ 0 & -S_{11} \end{pmatrix}, \tag{4.5}$$

whose eigenvectors and eigenvalues are the same as that of $\nabla \boldsymbol{v}$. This explains why scale separation holds even after vorticity-gradient sheets have been formed.

Figure 7 (plate 2) corresponds to a later time $t = 8$ within the k^{-3} regime. We see that the vorticity-gradient sheets are no longer isolated but have been packed together. Note that across layers that display very strong variation of vorticity, $\det(\nabla \boldsymbol{v})$ varies very smoothly. In the regions where strong (quasi-one-dimensional) layers are formed, vorticity is significantly smaller than strain, and we can locally approximate the velocity gradient by a constant strain, corresponding to a velocity field

$$u = -x, \quad v = y. \tag{4.6}$$

Vorticity is then viewed as a passive scalar and we can apply the Batchelor (1959) analysis (see also Leslie 1973), the relevance of which in the description of the enstrophy cascade was pointed out by Kraichnan (1975). Such a velocity field will pack together the vortex sheets in the direction of the y-axis. Furthermore, it is easy to write the equation satisfied by the correlation function of the vorticity field.

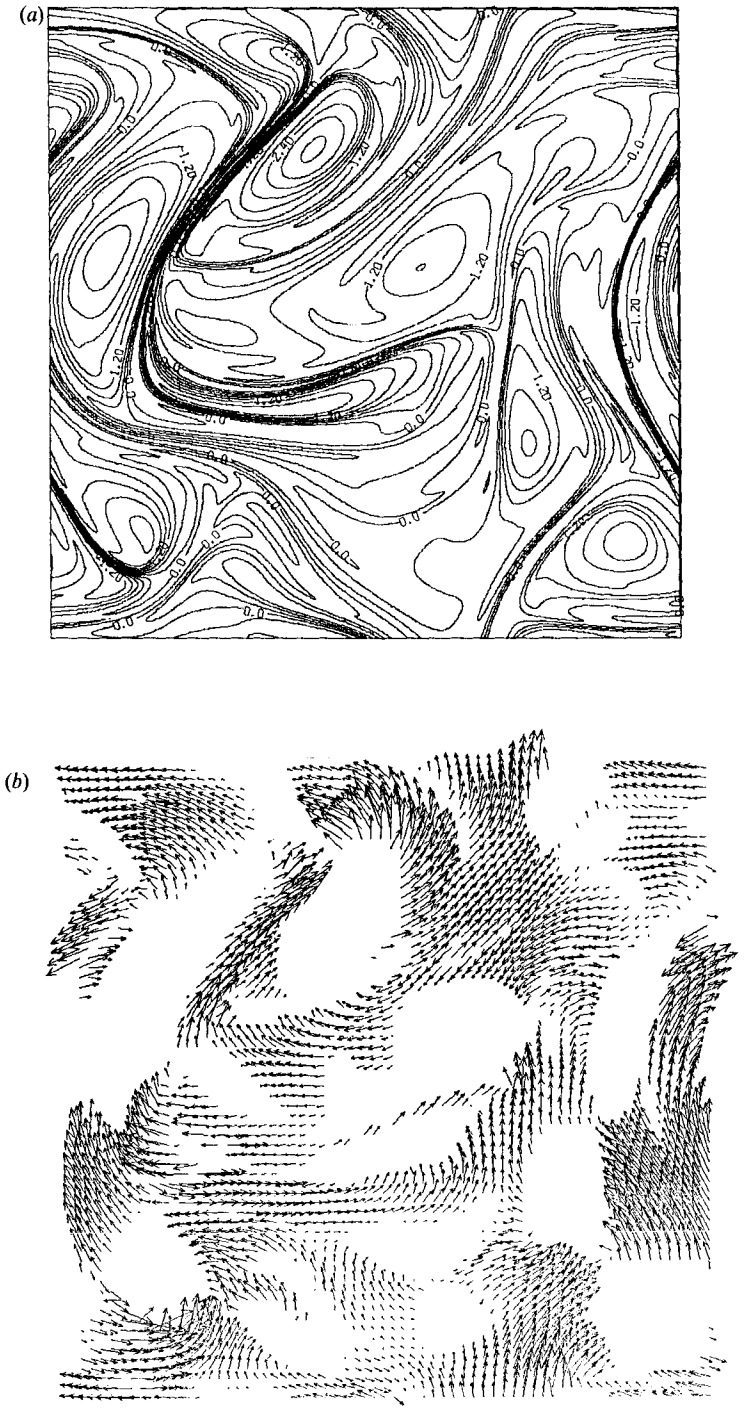

FIGURE 9. Space visualization for run P2-512 at $t = 7$: (*a*) isovorticity lines, (*b*) left eigenvector $\boldsymbol{l}^{(+)}$ of $(\nabla \boldsymbol{v})$ with positive real eigenvalue (when defined).

Assuming homogeneity and taking into account the one-dimensionality of the problem (to leading order), one has

$$\Omega(\xi, t) = < \omega(x, t)\, \omega(x+\xi, t) >, \tag{4.7}$$

which satisfies

$$\frac{\partial \Omega(\xi, t)}{\partial t} - \xi \frac{\partial \Omega(\xi, t)}{\partial \xi} + 2\nu \frac{\partial^2 \Omega(\xi, t)}{\partial \xi^2} = 0, \tag{4.8}$$

where ξ denotes the x-component of point separation. At scales large compared with the dissipative scales but small compared with the scales at which the sheets are generated, an equilibrium is established for which the vorticity spectrum $E_\omega(k, t)$ satisfies

$$\frac{\partial (k E_\omega(k))}{\partial k} = 0, \tag{4.9}$$

$$E_\omega(k) \sim 1/k, \tag{4.10}$$

which corresponds to an energy spectrum

$$E(k) \sim k^{-3}. \tag{4.11}$$

It is important to stress that in contrast with the Saffman theory, this Batchelor–Kraichnan analysis is statistical.

In addition to the vorticity-gradient sheets, the simulation also displays large-scale vortices. We see that these vortices are stretched when they are localized in a region of hyperbolic motion. When they move to regions of elliptic motion, their isotropy is restored. In this case neighbouring structures resulting from packing and reconnection of vorticity-gradient sheets are also subject to rotational motion and spin up around the coherent vortices. This phenomenon is clearly seen in figure 8, (plate 3) corresponding to a time $t = 13$. Again the local direction of the sheets is prescribed by the left eigenvector of $\nabla \boldsymbol{v}$ associated with the positive eigenvalue. In the simple case of a point vortex, the strain eigenvector associated with the positive eigenvalue will make an angle of $\frac{1}{4}\pi$ with the radius vector.

Throughout this section, we have asserted that the sheets are directed along the left eigenvector of $\nabla \boldsymbol{v}$ associated with the positive eigenvalue. This point is demonstrated in figure 9 which shows for the run P2-512 at time $t = 7$ both the vorticity field and the above eigenvector (where it is real). We see that the prediction is precisely verified.

5. Conclusion

We have presented in this paper direct numerical simulations of high-Reynolds-number turbulence. We were able to characterize precisely the inertial exponent of the energy spectrum which displays a transition from k^{-4} to k^{-3} when the turbulence becomes mature. In the first regime, the small scales consist of isolated vorticity-gradient sheets. In the second regime, the sheets are packed together and form more complex layers. In addition to these small-scale structures, the flow displays vorticity macro-eddies which appear to be very robust. We have validated the Weiss (1981) analysis of two-dimensional dynamics based on scale separation between velocity and vorticity gradients, and explained why this analysis remains valid even *after* vorticity-gradient sheets have been formed. In this approach, the local dynamics is completely prescribed by the sign of det $(\nabla \boldsymbol{v})$. Where det $(\nabla \boldsymbol{v})$ is negative, strain dominates and vorticity-gradient sheets are formed in the direction of the left

eigenvector associated with the positive eigenvalue of ∇v. Where it is positive, macro-eddies are stable. The model explains in particular the difference between the dynamical influence of pairs of vortices with opposite sign and with the same sign. In the former case a line of zero vorticity is present between them, and near this line vorticity-gradient sheets are formed. In contrast, two vortices with the same sign may either act as a rolling mill and generate vorticity-gradient sheets if strain dominates vorticity, or rotate around one another and eventually coalesce when the strain is weak. Such coalescence, as seen for example in the run P2-512, is shown in figure 9.

At later times than those we have reached in the simulations, the vorticity-gradient layers will be dissipated by viscosity and the dynamics will essentially reduce to that of coherent vortices which will persist for a very long time. This regime is difficult to investigate with high-resolution codes because of the prohibitive computer times that are required. Moderate resolutions are actually sufficient to investigate such a regime, in which the small scales have been rubbed out. A detailed investigation of the dynamics of the surviving vorticity macro-eddies has been carried out by McWilliams (1984).

We are grateful to C. Basdevant, U. Frisch, J. Herring, R. H. Kraichnan, S. A. Orszag, and R. Sadourny for useful discussions. Some of our computations were done on the CCVR Cray-1s at Palaiseau, using fast Fourier transforms written by S. A. Orszag and C. Temperton. We acknowledge partial support from a DRET contract and from the CNRS-ATP: 'Dynamique des fluides astro et géophysiques.'

REFERENCES

BASDEVANT, C., LEGRAS, B., SADOURNY, R. & BÉLAND, M. 1981 *J. Atmos. Sci.* **38**, 2305.

BATCHELOR, G. K. 1959 *J. Fluid Mech.* **5** 113.

BATCHELOR, G. K. 1969 *Phys. Fluids* **12**, 233.

BENZI, R., PATARNELLO, S. & SANTANGELO, P. 1987 *Europhys. Lett.* **3**, 811.

BRACHET, M. E., MEIRON, D. I., ORSZAG, S. A., NICKEL, B. G., MORF, R. H. & FRISCH, U. 1983 *J. Fluid Mech.* **130**, 411.

BRACHET, M. E., MENEGUZZI, M., POLITANO, H. & SULEM, P. L. 1986 In *Proc. European Turbulence Conference*. Proceedings in Physics. Springer (in press).

BRACHET, M. E., MENEGUZZI, M. & SULEM, P. L. 1985 In *Macroscopic Modeling of Turbulence Flow*. Lecture Notes in Physics vol. 230, p. 344, Springer.

BRACHET, M. E., MENEGUZZI, M. & SULEM, P. L. 1986 *Phys. Rev. Lett.* **57**, 683.

BRACHET, M. E. & SULEM, P. L. 1984 In *Proc. 9th Conf. on Numerical Methods in Fluid Mechanics*. Lecture Notes in Physics vol. 218, p. 103, Springer.

BRACHET, M. E. & SULEM, P. L. 1985 *Prog. Astron. Aeron.* **100**, 100.

DEEM, G. S. & ZABUSKY, N. J. 1971 *Phys. Rev. Lett.* **27**, 396.

FORNBERG, B. 1977 *J. Comp. Phys.* **25**, 1.

FRISCH, U., POUQUET, A., SULEM, P. L. & MENEGUZZI, M. 1983 *J. Méc. Théor. Appl. Numéro Spéciale, 2D. Turbulence*, p. 191.

FRISCH, U. & SULEM, P. L. 1984 *Phys. Fluids* **27**, 1921.

FYFE, D., MONTGOMERY, D. & JOYCE, G. 1977 **117**, 369.

GOTTLIEB, D. & ORSZAG, S. A. 1977 *Numerical Analysis of Spectral Methods: Theory and Applications*. SIAM.

HERRING, J. R. 1975 *J. Atmos. Sci.* **32**, 2254.

HERRING, J. R. & MCWILLIAMS, J. C. 1985 *J. Fluid Mech.* **153**, 229.

HERRING, J. R., ORSZAG S. A., KRAICHNAN, R. H. & FOX, D. G. 1974 *J. Fluid Mech.* **66**, 417.

KIDA, S. 1981 *Phys. Fluids* **24**, 604.

KIDA, S. 1985 *J. Phys. Soc. Japan* **54**, 2840.

KIDA, S. & YAMADA, M. 1984 In *Turbulence and Chaotic Phenomena in Fluids* (ed. T. Tatsumi). Elsevier.

KRAICHNAN, R. H. 1967 *Phys. Fluids* **10**, 1417.

KRAICHNAN, R. H. 1971 *J. Fluid Mech.* **47**, 525.

KRAICHNAN, R. H. 1975 *J. Fluid Mech.* **67**, 155.

LEGRAS, B., SANTANGELO, P. & BENZI, R. 1988 High resolution numerical experiments for forced two-dimensional turbulence. *Europhys. Lett.*, **5**, 37.

LEITH, C. 1968 *Phys. Fluids* **11**, 671.

LESIEUR, M. 1987 *Turbulence in Fluids*. Nijhoff.

LESLIE, D. C. 1973 *Developments in the Theory of Turbulence*, Clarendon.

LILLY, D. K. 1969 *Phys. Fluids Suppl.* **12**, 11, 240.

LILLY, D. K. 1971 *J. Fluid Mech.* **45**, 395.

LILLY, D. K. 1972 *Geophys. Fluid Dyn.* **3**, 289; **4**, 1.

MANDELBROT, B. 1976 In *Turbulence and Navier–Stokes equation*. Lecture Notes in Mathematics vol. 565, p. 121. Springer.

MCWILLIAMS, J. C. 1984 *J. Fluid Mech.* **146**, 21.

ORSZAG, S. A. 1977 In *Proc. 5th Intl. Conf. on Numerical Methods in Fluids Dynamics* Lecture Notes in Physics, vol. 59, p. 32.

POUQUET, A., LESIEUR, M., ANDRÉ, J. C. & BASDEVANT, C. 1975 *J. Fluid Mech.* **72**, 305.

SAFFMAN, P. G. 1971 *Stud. Appl. Maths* **50**, 377.

SULEM, C., SULEM, P. L. & FRISCH, H. 1983 *J. Comp. Phys.* **50**, 138.

TATSUMI, T. & YANASE, S. 1981 *J. Fluid Mech.* **110**, 475.

WEISS, J 1981 The dynamics of enstrophy transfer in two-dimensional hydrodynamics, LJI-TN-81-121. La Jolla Inst. La Jolla, California.